

# HCS-TNAS: Hybrid Constraint-driven Semi-supervised Transformer-NAS for Ultrasound Image Segmentation

Renqi Chen

23210860007@m.fudan.edu.cn

Academy for Engineering & Technology, Fudan University  
Shanghai, China

## ABSTRACT

Accurate ultrasound segmentation is pursued because it aids clinicians in achieving a comprehensive diagnosis. Due to the presence of low image quality and high costs associated with annotation, two primary concerns arise: (1) enhancing the understanding of multi-scale features, and (2) improving the resistance to data dependency. To mitigate these concerns, we propose HCS-TNAS, a novel neural architecture search (NAS) method that automatically designs the network. For the first concern, we employ multi-level searching encompassing cellular, layer, and module levels. Specifically, we design an Efficient NAS-ViT module that searches for multi-scale tokens in the vision Transformer (ViT) to capture context and local information, rather than relying solely on simple combinations of operations. For the second concern, we propose a hybrid constraint-driven semi-supervised learning method that considers additional network independence and incorporates contrastive loss in a NAS formulation. By further developing a stage-wise optimization strategy, a rational network structure can be identified. Extensive experiments on three publicly available ultrasound image datasets demonstrate that HCS-TNAS effectively improves segmentation accuracy and outperforms state-of-the-art methods.

## CCS CONCEPTS

• **Computing methodologies** → **Computer vision.**

## KEYWORDS

Semi-supervised learning, NAS, Searchable Transformer

## 1 INTRODUCTION

Echocardiography (cardiovascular ultrasound) is a critical medical imaging tool for diagnosing cardiac diseases, and achieving precise segmentation of echocardiographic images can further assist clinicians in comprehensively analyzing cardiac conditions [15]. However, segmentation algorithms face challenges such as the lack of annotated data, speckle noise in ultrasound images, and the difficulty in discriminating adjacent anatomical structures [38], which necessitates (1) the understanding of multi-scale features, and (2) robustness to data dependency.

Over the past years, the development of deep learning (DL) in medical image segmentation has represented a progression in understanding multi-scale features. Yu et al. [33] first introduced dynamic convolutional neural networks for fetal left ventricle segmentation, aiming to maximize the effectiveness of local feature perception. With the proposal of U-Net [24], which exhibited extraordinary feature extraction ability, the U-shaped encoder-decoder network garnered attention and spawned multiple variants, such as UNet++ [39]. Inspired by this, the Res-U network [1] combines ResNet [10]

**Table 1: Comparison with four types of mainstream methods from the perspectives of the key concerns. “Multi-scale” denotes the consideration of multi-scale features and “Dependency” denotes the degree of data dependency. “Fully” and “Semi” denote fully-supervised and semi-supervised models, respectively. “Manual” and “NAS” indicate whether the model structure is manually designed or optimized via neural architecture search, respectively. “✓” and “○” denote conformity.**

Method	Multi-scale	Dependency
Fully & Manual <i>e.g.</i> , Transfuse [37]	✓ (Rigorous design)	○○
Fully & NAS <i>e.g.</i> , M <sup>3</sup> NAS [18]	✓	○○
Semi & Manual <i>e.g.</i> , UA-MT [34], URPC [19]	-	○
Semi & NAS <i>e.g.</i> , Se <sup>2</sup> NAS [21]	✓	○
<b>Semi &amp; NAS, Ours</b>	✓✓	○

and U-Net, generating reliable results by leveraging skip connections within functional blocks to extract accessible features. While these works focus on local feature perception, the vision Transformer (ViT) [9] was proposed with a strong context-sensing ability to capture the relationship between distant pixels. Subsequently, Chen et al. [6] proposed TransUNet, which combines a U-shaped network with the Transformer. Cai et al. proposed EfficientViT [5], which employs ReLU linear attention in the ViT to enhance the model’s capability while reducing the number of parameters.

While handcrafted networks necessitate a substantial level of expertise to design a rational structure for understanding multi-scale features, neural architecture search (NAS) has garnered attention as it enables automatic optimization of network structures within the provided search space. Grounded in the concept of hierarchical structure, Auto-DeepLab [16] was proposed to search for network backbones across multiple levels, achieving commendable performance on large-scale general datasets. Ren et al. [23] also employed NAS for left ventricular myocardium segmentation. However, the current NAS methods applied to ultrasound image segmentation tend to blindly expand the search space while neglecting efficiency, resulting in heavy parameter loads but marginal improvements.

On the other hand, medical image datasets often suffer from a scarcity of labeled data, causing traditional supervised models to exhibit a high degree of data dependency and fail to achieve satisfactory results. Hence, unlabeled data needs to be utilized for

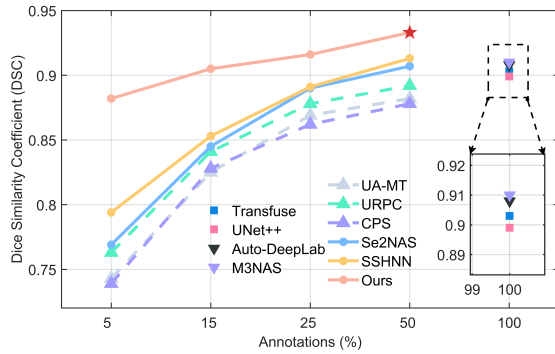


**Figure 1: Comparison with the state-of-the-art methods from the perspective of performance on the CETUS dataset [4]. We outperform the current best-performing semi-supervised method SSHNN [7] around 2.00% in the DSC metric.**

segmentation tasks, and semi-supervised learning (SSL) provides an excellent solution. Current SSL methods, such as Mean Teacher [26] and co-training [8], efficiently enhance model robustness against data dependency and have been employed for echocardiographic segmentation. Wu et al. [29] designed an adaptive spatiotemporal semantic calibration algorithm for their semi-supervised model, achieving satisfactory performance. After years of research, it has then been noticed that combining NAS and SSL can be meaningful. Pauletto et al. [21] demonstrated the effectiveness of this idea by proposing a self-semi-supervised NAS for accurate semantic segmentation. Nonetheless, semi-supervised NAS still holds research potential, as previous work has merely involved rudimentary stitching, treating this concept superficially. Inspired by CauSSL [20], which additionally considered the algorithmic independence of the model on top of the co-training framework and got outstanding results, we begin considering designing hybrid constraint-driven semi-supervised learning for the NAS model, leveraging the distinctive network characteristics of NAS.

Based on the above analysis, we propose HCS-TNAS, a hybrid constraint-driven semi-supervised Transformer neural architecture search, for ultrasound image segmentation. We summarize the differences between our method and seminal methods in Tab. 1. For the issue of multi-scale feature extraction and understanding, we implement hierarchical NAS, searching for the optimal structure at the cellular, layer, and module (i.e., encoder and decoder) levels. At the basic cellular layer, we propose an Efficient NAS-ViT module that combines NAS with ViT for multi-scale token processing while mitigating the issue of excessive parameters caused by using the Transformer. At the layer level, we use feature fusion blocks to aggregate multi-resolution features. At the module level, we design NAS in both the encoder and decoder with specific search spaces to ensure their respective functionalities. For the issue of data dependency, different from existing semi-supervised NAS methods, we consider multiple constraints on top of the co-training framework, including network independence loss and contrastive loss. The network independence loss encourages the two co-trained models to be algorithmically independent, providing complementary

assistance to each other [20]. Additionally, contrastive loss assists in maximizing mutual information across different views of the same image [2] from complementary networks. Our performance comparison with other models is shown in Fig. 1.

In summary, the main contributions of this paper are as follows:

(1) We propose a Hybrid Constraint-driven Semi-supervised Transformer-NAS, termed HCS-TNAS, for accurate ultrasound image segmentation. The two main issues are concluded: the multi-scale feature understanding, and the data dependency.

(2) We adopt multi-level searching for the issue of the multi-scale feature understanding. Specifically, we design an Efficient NAS-ViT module to generate multi-scale tokens. To the best of our knowledge, this is the first study that introduces NAS into the ViT for token-level searching, departing from the linear combination of features in existing works.

(3) We propose a hybrid constraint-driven SSL for the issue of data dependency. Building upon the co-training, we incorporate algorithmic independence and contrastive learning into the unique multi-stage optimization of NAS, thereby maximizing the utilization of spatial and geometric information for feature discrimination.

(4) We conduct extensive experiments on three public ultrasound image datasets, demonstrating the advancement of HCS-TNAS.

## 2 RELATED WORK

### 2.1 Neural Architecture Search

NAS is proposed to resolve the difficulty of network design and find the optimal network architecture within the search space. After the introduction of differentiable architecture search (DARTS) [17], which created a continuous relaxation algorithm to provide differentiable candidate operation weights, gradient-based NAS became trainable on a single GPU, alleviating the high computational complexity and time overhead issues. As a DARTS variant, PC-DARTS [31] proposed two new techniques: partial channel connections and edge normalization, further reducing GPU memory consumption. Edge normalization also inspired the development of hierarchical NAS (HNAS), enabling a multi-level search. Liu et al. [16] first proposed Auto-DeepLab, which optimizes the network at the cell and layer levels. In DCNAS [36], Zhang et al. incorporated skip connections into HNAS to promote model capacity. Moreover, the Transformer is also used in HNAS to compensate for the lack of context information. In HCT-Net [35], Yu et al. utilized a Transformer to process feature maps of varying resolutions. Yang et al. proposed DAST [32] which incorporates the Transformer layer as candidate operations for cell-level searching.

In contrast to these NAS works, we search architecture from three levels: cell, layer, and encoder-decoder, allowing for higher degrees of freedom. Specifically, to mitigate the issue of excessive parameters caused by the Transformer and facilitate better multi-scale feature understanding, we creatively implement NAS in ViT for multi-scale tokens rather than relying on mixed feature maps.

### 2.2 SSL for Medical Image Segmentation

SSL can alleviate the scarcity of labeled data in medical image segmentation, which can be broadly categorized into pseudo-labeling methods and consistency regularization methods. Pseudo-labeling

method produces pseudo-labels for unlabeled data for refining accurate segmentation results. Bai et al. [3] proposed a self-training framework for cardiac MRI segmentation. The network predictions for unlabeled data were treated as pseudo labels and network parameters were iteratively updated. In [27], SSL was enhanced by adopting uncertainty-guided confidence-aware refinement at the pixel level to promote pseudo-label precision and leveraging image-level uncertainty to mitigate the influence of low-quality pseudo labels. For consistency regularization methods, Tarvainen et al. [26] proposed mean teacher (MT), which averaged weight parameters to form a target-generating teacher model for promoting the consistency between predictions and targets. Building upon this, Yu et al. [34] proposed a novel uncertainty-aware mean teacher (UA-MT) framework for left atrium segmentation. Apart from the popular MT framework, Qiao et al. [22] proposed the Deep co-training framework, which trained multiple networks to provide different and complementary information regarding the data. Xia et al. [30] developed the uncertainty-aware multi-view co-training (UMCT), proving the effectiveness of multi-view consistency in co-training.

In our work, we opt to design a hybrid constraint-driven SSL framework, tailored for NAS. Building upon the co-training, we first introduce network independence loss for multi-view consistency and show its utility for NAS. Furthermore, we ingeniously leverage the hierarchical architecture of the decoder NAS to define additional contrastive loss, maximizing mutual information from the diverse perspectives generated by complementary networks.

## 3 METHOD

### 3.1 Overview

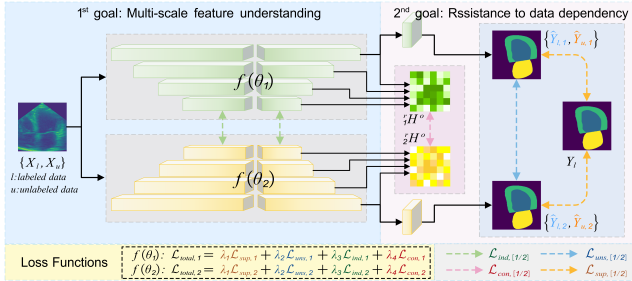


**Figure 2: The pipeline of our HCS-TNAS framework. Two networks are optimized by minimizing the combination of the supervised loss  $\mathcal{L}_{sup}$  on labeled data, the unsupervised loss  $\mathcal{L}_{uns}$  on unlabeled data, the contrastive loss  $\mathcal{L}_{con}$  on feature maps, and the network independence loss  $\mathcal{L}_{ind}$  on network parameters.**

An overview of the proposed HCS-TNAS is provided in Fig. 2. Our framework uses two neural networks based on the co-training framework: a Student network  $f(\theta_1)$  and a Teacher network  $f(\theta_2)$ , where both networks share the same HNAS-based backbone but use different parameters and independent optimizers. Our HNAS backbone comprises two parts: an encoder NAS and a decoder NAS, with further details presented in Sec. 3.3. To explore a novel approach that integrates NAS with ViT for global context modeling,

**Table 2: Cell candidate operations.**

Candidate Operations	Encoder Cell	Decoder Cell
3×3 separable convolution	✓	✓
5×5 separable convolution	✓	✓
3×3 convolution with dilation rate 2	✓	✓
5×5 convolution with dilation rate 2	✓	✓
3×3 average/max pooling	✓	✗
skip connection	✓	✓
no connection (zero)	✓	✗

we propose an Efficient NAS-ViT module (Sec. 3.2) in NAS backbone, in contrast to linear combinations of feature maps (after candidate operations) in existing works. Moreover, the encoder and decoder consider different sets of candidate operations, as shown in Table 2. Instead of the Mean Teacher, we adopt a hybrid constraint-driven SSL method (Sec. 3.4) on top of the co-training framework to update network parameters. The overall loss function is represented by:

$$\mathcal{L}_{total,i} = \lambda_1 \mathcal{L}_{sup,i} + \lambda_2 \mathcal{L}_{uns,i} + \lambda_3 \mathcal{L}_{ind,i} + \lambda_4 \mathcal{L}_{con,i} \quad (1)$$

where  $i \in 1, 2$ , corresponds to  $f(\theta_1)$  and  $f(\theta_2)$ , respectively,  $\mathcal{L}_{sup,i}$  is the supervised loss, which is the combination of the cross-entropy loss and the Dice loss calculated from the predictions  $p_l$  and the ground truth labels  $y_l$  on the labeled dataset:

$$\mathcal{L}_{sup,i} = \frac{1}{2} [l_{ce}(p_{l,i}, y_{l,i}) + l_{dice}(p_{l,i}, y_{l,i})], \quad (2)$$

and  $\mathcal{L}_{uns,i}$  is the unsupervised loss,  $\mathcal{L}_{ind,i}$  is the network independence loss, and  $\mathcal{L}_{con,i}$  is the contrastive loss. The details are provided in Sec. 3.4.  $\lambda_1, \lambda_2, \lambda_3$  and  $\lambda_4$  are hyper-parameters.

### 3.2 Efficient NAS-ViT Module

In DAST [32], the ViT layer is directly added to candidate operations, leading to increased computation complexity. On the other hand, since the ViT is more complex than other operations, the model tends to favor selecting the ViT during backbone optimization, rendering the search less meaningful. To resolve this issue, we replace it with EfficientViT [5] as a base module, further implementing NAS before attention calculation for searching multi-scale tokens and reducing excessive parameter overhead, termed Efficient NAS-ViT. It will be used in the inner cell search of the encoder NAS and the effectiveness of this novel Transformer-based approach for NAS will be shown through the empirical results of Sec. 4.4. An overview of the Efficient NAS-ViT is illustrated in Fig. 3 (d), featuring the NAS-based Multi-scale Linear Attention, which integrates NAS with ReLU linear attention. The FFN+DWConv refers to the application of depthwise convolution on the FFN layer.

Given input  $x \in \mathbb{R}^{N \times f}$  after linear projection, tokens  $Q = xW_Q$ ,  $K = xW_K$ ,  $V = xW_V$ , where  $W_Q/W_K/W_V \in \mathbb{R}^{f \times d}$  is the learnable linear projection matrix. Instead of using fixed operations to obtain multi-scale tokens in the original work, which constrains the token representation and affects attention calculation, we leverage the NAS technique to search for token representations, thereby enhancing the multi-scale learning capacity. By incorporating partial channel connections to reduce memory overhead and reusing continuous relaxation for a differentiable search space, the multi-scale

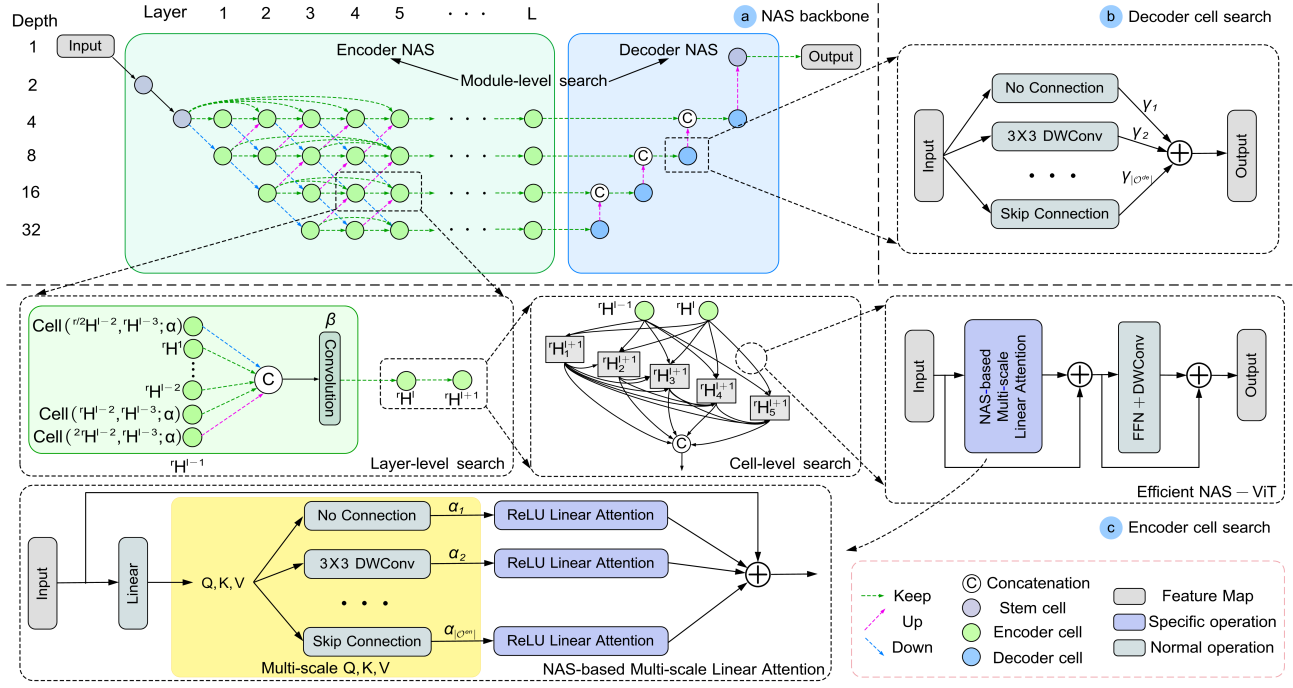


**Figure 3: The details of our proposed NAS backbone. (a) shows an overview of the NAS backbone, which consists of an encoder NAS and a decoder NAS, representing a module-level search. The input is passed through the encoder NAS to obtain multi-resolution feature maps, where a hierarchical encoder cell search is performed (shown in (c)). These outcomes are then processed by the decoder cells (shown in (b)), which concatenate features and complete the recovery process through further searching.**

tokens  $Q'/K'/V'$  are formulated as:

$$\{Q'/K'/V'\} = \sum_{O_k \in \mathcal{O}^{en}} \frac{\exp\{\alpha_k\}}{\sum_{m=1}^{|\mathcal{O}^{en}|} \exp\{\alpha_m\}} \cdot O_k(\mathbf{P} \circ \{Q/K/V\}) + (1 - \mathbf{P}) \circ \{Q/K/V\}, \quad (3)$$

where  $\mathbf{P}$  is the sampling mask for channel selection,  $O_k$  denotes the  $k^{\text{th}}$  operation selected from the set of encoder candidate operations  $\mathcal{O}^{en}$ , and  $\alpha_k$  is cell architecture parameter after applying the softmax, which measures the weight of related candidate operation.

Subsequently, tokens are computed by ReLU linear attention:

$$O_n = \sum_{j=1}^N \frac{\text{ReLU}(Q_n)\text{ReLU}(K_j)^T}{\sum_{j=1}^N \text{ReLU}(Q_n)\text{ReLU}(K_j^T)} V_j \quad (4)$$

where  $O_n$  denotes the  $n^{\text{th}}$  row of  $O$ . Benefiting from the attention mechanism, ReLU linear attention captures contextual information. Then, the output is fed into the FFN+DWConv layer, which captures local information.

### 3.3 NAS Backbone

**3.3.1 Encoder NAS.** It comprises cell- and layer-level searches, which encompass a larger search space for multi-scale feature extraction. Regarding the cell, there are  $N$  intermediate nodes in cell search space, where the edge between nodes corresponds to the proposed Efficient NAS-ViT module, shown in the Right of Fig. 3(c). After processing the inputs by Efficient NAS-ViT, the output of the

$n^{\text{th}}$  node of the encoder cell in the  $l^{\text{th}}$  layer is:

$$H_n^l = \sum_{H_j^l \in \mathcal{I}} \text{Efficient NAS - ViT}(H_j^l; \alpha) \quad (5)$$

where the inputs  $H_j^l \in \mathcal{I}$  includes the previous cell's output and previous nodes' output in the current cell. The final output tensor of the cell is the concatenation of outputs from all nodes (shown in the Middle of the Fig. 3). For simplicity, the cell-level search is written as:

$$H^l = \text{Cell}(H^{l-1}, H^{l-2}; \alpha). \quad (6)$$

The layer-level search aims at aggregating features from different resolutions by employing convolution kernels and skip connections, illustrated in the Left of the Fig. 3. The parameters of these kernels are referred to as the architecture parameters  $\beta$ . There are  $L$  layers in the backbone. To capture multi-resolution features, our model considers six resolutions:  $r = 1, 2, 4, 8, 16, 32$ , where  $r = 1$  corresponds to the original image size. When  $r = 4$ , the spatial size of the feature maps is 1/4 of the case where  $r = 1$ . The formulation of the  $l^{\text{th}}$  layer level search is denoted as:

$$\begin{aligned} {}^r H^l = & \text{Conv}(\text{Concat}[\text{Down}(\text{Cell}(\frac{r}{2} H^{l-1}, r H^{l-2}; \alpha)), \\ & \text{Up}(\text{Cell}({}^{2r} H^{l-1}, r H^{l-2}; \alpha)), \text{Cell}(r H^{l-1}, r H^{l-2}; \alpha), \\ & \{r H^{l'} \in {}^r H | l' < l\}], \end{aligned} \quad (7)$$

where  $\text{Cono}(\cdot)$  denotes the convolution, transforming fused features to the same channel counts of  $r$ -resolution,  $\text{Down}(\cdot)$  denotes downsampling, and  $\text{Up}(\cdot)$  denotes upsampling.

**3.3.2 Decoder NAS.** Instead of employing fixed convolution kernel sizes, we introduce NAS for the decoder design to enhance the capability. The set of candidate operations  $\mathcal{O}^{de}$  for the decoder is presented in Table 8. Specifically, a U-shaped architecture is used as the backbone for the decoder NAS, as depicted in Fig. 3(a).

In the decoder NAS, the features from the  $r = 32$  layer after the encoder NAS are fed into the decoder cell as the initial input. To mitigate the excessive computational complexity introduced by NAS, the decoder cell does not contain any intermediate nodes, as shown in Fig. 3(b). The search can be denoted as:

$${}^r H^o = \sum_{O_k \in \mathcal{O}^{de}} \frac{\exp\{\gamma_k\}}{\sum_{m=1}^{|\mathcal{O}^{de}|} \exp\{\gamma_m\}} \cdot O_k({}^r H^{l=L}), \quad (8)$$

where  $\gamma$  are decoder architecture parameters, and  ${}^r H^o$  is the final output tensor of decoder cell in  $r$ -resolution.

After upsampling, the features  ${}^r H^o$  are concatenated with  ${}^{r/2} H^L$ , and a convolution layer is applied to match the number of channels with the  $r/2$  decoder NAS. This process is then repeated until the  $r = 4$  features are combined. Finally, an upsample layer is employed to recover the outputs to the full resolution, followed by a convolution layer to obtain the desired number of classes for segmentation tasks.

### 3.4 Hybrid Constraints-driven SSL

Owing to the challenges of annotating medical images, public datasets typically comprise a substantial amount of unlabeled data and a limited amount of labeled data. To leverage the unlabeled data, the co-training framework of SSL is implemented, where the unsupervised loss is defined as:

$$\mathcal{L}_{uns,i} = l_{ce}(p_{u,i}, \hat{y}_{u,3-i}) \quad (9)$$

where  $p_{u,i}$  is the predicted probability maps generated by one network on the unlabeled data, and  $\hat{y}_{u,3-i}$  is the corresponding one-hot pseudo label generated by the other network:

$$\hat{y}_{u,i} = \arg \max_C \{p_{u,i}\} \quad (10)$$

Through the analysis in SSL [20], the algorithmic independence property has been demonstrated to facilitate the creation of two distinct networks, especially in the co-training. Complementary networks are capable of capturing diverse feature information and contributing to the segmentation accuracy promotion. Thus, we incorporate network independence loss and propose a stage-wise optimization strategy (Sec 3.5) to fulfill this potential. We define the network dependence between two NAS backbones based on the convolutional layers at the same position as follows:

$$\mathcal{L}_{ind,i} = \frac{1}{\sum layers} \sum_{k=1}^{\sum layers} l_{ind}(\theta_{i,k}, \theta_{3-i,k}; G_{3-i,k}) \quad (11)$$

where  $\sum layers$  denotes the total number of convolutional layers.  $\theta_{1/2,k} \in \mathbb{R}^{C_{out} \times (N \times N \times C_{in})}$  are the weight parameters of the  $k^{th}$  convolutional layer for two networks, which are reshaped into a matrix form  $\mathbb{R}^{C_{out} \times d}$  ( $d = N \times N \times C_{in}$ ) for loss calculation, where  $N$  is the kernel size,  $C_{in}$  is the number of input feature channels

and  $C_{out}$  corresponds to the number of output feature channels.  $\{G_{1,k}, G_{2,k}\} \in \mathbb{R}^{C_{out} \times C_{out}}$  are the corresponding optimal coefficient matrix. The network independence loss  $l_{ind}$  is defined as:

$$l_{ind}(A, B; G_B) = \frac{1}{C_{out}} \sum_{k=1}^{C_{out}} \left( \frac{\mathbf{v}_{A,k} \cdot \mathbf{q}_{B,k}}{|\mathbf{v}_{A,k}| \times |\mathbf{q}_{B,k}|} \right)^2 \quad (12)$$

$$\mathbf{q}_{B,k} = (G_B \times B)_k$$

where  $\mathbf{v}_{A,k}$  is the  $k^{th}$  row vector of matrix  $A$ , and  $\mathbf{q}_{B,k}$  is the vector obtained by performing linear combination on  $B$  using the  $G_B$ . The network independence is summarized as a min-max optimization:

$$\min_{\theta_1, \theta_2} \max_{G_1, G_2} \mathcal{L}_{ind,1}(\theta_1, \theta_2; G_2) + \mathcal{L}_{ind,2}(\theta_2, \theta_1; G_1) \quad (13)$$

Since algorithmic independence essentially endows the network with the capability to observe the same image from different perspectives, contrastive loss [2, 11] is utilized as an additional constraint to maximize the mutual information across these views. Benefiting from network independence, there is no need to construct an asymmetric architecture for contrastive loss.

In this work, an uncertainty-based contrastive loss is creatively proposed in the form of NAS, measured on the outputs at different stages of the decoder cell between two networks. The uncertainty estimation is defined using smoothed KL-divergence to avoid singular values and consider features at various resolutions as follows:

$$U_i^{r,h,w} = \sum_{c=0}^{C-1} ({}^r H^o)^{c,h,w} \cdot \log \frac{({}^r H^o)^{c,h,w} + \epsilon}{(\overline{{}^r H^o})^c + \epsilon} \quad (14)$$

where  $C$  is the channel dimension,  $\epsilon$  is a small bias term,  $r \in \{4, 8, 16, 32\}$  are used,  ${}^r_1 H^o$  and  ${}^r_2 H^o$  are the output tensors of the decoder cell at the  $r$ -resolution for  $f(\theta_1)$  and  $f(\theta_2)$ , respectively.  $\overline{(\cdot)}$  is the mean value across the channel dimension. A higher estimation value reflects a higher uncertainty, which can be used to compel the lower-quality features to align with their higher-quality counterparts.

Consequently, the positions of these features are estimated by:

$$\mathcal{P}_i^{r,h,w} = \mathbf{1} \circ \{U_i^{r,h,w} > U_{3-i}^{r,h,w}\} \quad (15)$$

where  $\circ$  denotes Hadamard product and contrastive loss  $\mathcal{L}_{con}$  is:

$$\mathcal{L}_{con,i} = \sum_{r \in \{4,8,16,32\}} \sum_{p \in \mathcal{P}_i^{r,h,w}} l_{mse}(({}^r_1 H^o)^p, ({}^r_2 H^o)^p) \quad (16)$$

### 3.5 Stage-wise Optimization Strategy

To adapt to the hybrid constraint-driven SSL, we propose a stage-wise optimization strategy, summarized in Alg. 1. In each iteration, we first fix the network parameters and optimize the combination matrix for  $E_B$  epochs. In the second stage, we fix the combination matrix and network architecture parameters and then update the network weights by minimizing  $L_{total}$ . In the third stage, we only update the architecture parameters by minimizing  $L_{total}$  after  $E_A$  epochs. During the optimization, continuous relaxation is implemented for the gradient descent algorithm.

**Table 3: Comparison with SOTAs on the CAMUS, HMC-QU, and CETUS datasets. SSL methods are tested on 50% labeled data.**

Learning Paradigm	Design Strategy	Method	HMC-QU			CETUS			CAMUS		
			DSC↑	IoU↑	95HD↓	DSC↑	IoU↑	95HD↓	DSC↑	IoU↑	95HD↓
Fully (100%)	Manual	UNet++ [39]	0.899 <sub>(0.005)</sub>	0.898 <sub>(0.004)</sub>	4.860 <sub>(0.102)</sub>	0.952 <sub>(0.002)</sub>	0.968 <sub>(0.001)</sub>	2.386 <sub>(0.091)</sub>	0.919 <sub>(0.006)</sub>	0.855 <sub>(0.009)</sub>	6.584 <sub>(0.578)</sub>
		nnU-Net [12]	0.908 <sub>(0.005)</sub>	0.907 <sub>(0.005)</sub>	3.843 <sub>(0.310)</sub>	0.958 <sub>(0.001)</sub>	0.970 <sub>(0.001)</sub>	2.099 <sub>(0.048)</sub>	0.922 <sub>(0.003)</sub>	0.860 <sub>(0.004)</sub>	6.075 <sub>(0.412)</sub>
		Transfuse [37]	0.903 <sub>(0.004)</sub>	0.903 <sub>(0.004)</sub>	4.304 <sub>(0.228)</sub>	0.957 <sub>(0.002)</sub>	0.971 <sub>(0.001)</sub>	2.152 <sub>(0.102)</sub>	0.923 <sub>(0.004)</sub>	0.861 <sub>(0.006)</sub>	5.853 <sub>(0.496)</sub>
	NAS	Auto-DeepLab [16]	0.908 <sub>(0.004)</sub>	0.907 <sub>(0.004)</sub>	3.857 <sub>(0.164)</sub>	0.954 <sub>(0.004)</sub>	0.968 <sub>(0.001)</sub>	2.278 <sub>(0.133)</sub>	0.918 <sub>(0.003)</sub>	0.851 <sub>(0.006)</sub>	6.641 <sub>(0.473)</sub>
		M <sup>3</sup> NAS [18]	0.910 <sub>(0.007)</sub>	0.909 <sub>(0.006)</sub>	3.709 <sub>(0.288)</sub>	0.956 <sub>(0.005)</sub>	0.969 <sub>(0.001)</sub>	2.175 <sub>(0.174)</sub>	0.920 <sub>(0.004)</sub>	0.856 <sub>(0.004)</sub>	6.405 <sub>(0.556)</sub>
		NasUNet [28]	0.884 <sub>(0.006)</sub>	0.881 <sub>(0.005)</sub>	6.374 <sub>(0.257)</sub>	0.944 <sub>(0.003)</sub>	0.965 <sub>(0.002)</sub>	3.191 <sub>(0.129)</sub>	0.914 <sub>(0.004)</sub>	0.845 <sub>(0.005)</sub>	6.962 <sub>(0.552)</sub>
Semi (50%)	Manual	UA-MT [34]	0.882 <sub>(0.005)</sub>	0.880 <sub>(0.006)</sub>	6.522 <sub>(0.199)</sub>	0.947 <sub>(0.003)</sub>	0.964 <sub>(0.002)</sub>	3.034 <sub>(0.106)</sub>	0.908 <sub>(0.002)</sub>	0.837 <sub>(0.002)</sub>	7.440 <sub>(0.161)</sub>
		URPC [19]	0.892 <sub>(0.004)</sub>	0.891 <sub>(0.004)</sub>	5.355 <sub>(0.125)</sub>	0.941 <sub>(0.004)</sub>	0.963 <sub>(0.003)</sub>	3.374 <sub>(0.185)</sub>	0.912 <sub>(0.002)</sub>	0.842 <sub>(0.002)</sub>	6.708 <sub>(0.152)</sub>
		CPS [8]	0.878 <sub>(0.005)</sub>	0.877 <sub>(0.005)</sub>	6.908 <sub>(0.296)</sub>	0.923 <sub>(0.005)</sub>	0.954 <sub>(0.003)</sub>	4.306 <sub>(0.282)</sub>	0.901 <sub>(0.004)</sub>	0.827 <sub>(0.005)</sub>	8.864 <sub>(0.477)</sub>
	NAS	Se <sup>2</sup> NAS [21]	0.907 <sub>(0.004)</sub>	0.907 <sub>(0.004)</sub>	3.941 <sub>(0.303)</sub>	0.955 <sub>(0.003)</sub>	0.967 <sub>(0.003)</sub>	2.235 <sub>(0.111)</sub>	0.920 <sub>(0.002)</sub>	0.856 <sub>(0.003)</sub>	6.410 <sub>(0.311)</sub>
		SSHNN-L [7]	0.913 <sub>(0.002)</sub>	0.912 <sub>(0.002)</sub>	3.611 <sub>(0.145)</sub>	0.959 <sub>(0.002)</sub>	0.971 <sub>(0.001)</sub>	2.053 <sub>(0.087)</sub>	0.929 <sub>(0.002)</sub>	0.868 <sub>(0.003)</sub>	5.516 <sub>(0.278)</sub>
		<b>HCS-TNAS</b>	<b>0.933<sub>(0.002)</sub></b>	<b>0.931<sub>(0.002)</sub></b>	<b>2.480<sub>(0.161)</sub></b>	<b>0.972<sub>(0.001)</sub></b>	<b>0.978<sub>(0.001)</sub></b>	<b>1.620<sub>(0.036)</sub></b>	<b>0.937<sub>(0.002)</sub></b>	<b>0.884<sub>(0.003)</sub></b>	<b>5.042<sub>(0.168)</sub></b>

**Algorithm 1** Optimization Strategy

**Input:** Datasets  $\mathcal{D}_l, \mathcal{D}_u$ , weights  $w$ , architecture parameters  $\alpha, \beta, \gamma$ , combination matrices  $G_1, G_2$ , alpha epoch  $E_A$ , beta epoch  $E_B$

**Output:** Searched  $f(\theta_1^*), f(\theta_2^*)$

- 1: **for**  $e = 1, \dots, E$  **do**
- 2:   **for**  $f = 1, \dots, E_B$  **do**
- 3:     Fix  $w, \alpha, \beta, \gamma$ . Update  $G_1, G_2$  by maximizing  $\mathcal{L}_{ind,1}$  and  $\mathcal{L}_{ind,2}$ , respectively.
- 4:   **end for**
- 5:   Fix  $G_1, G_2, \alpha, \gamma$ . Update  $w$  and  $\beta$  of  $f(\theta_1)$  and  $f(\theta_2)$  by minimizing  $\mathcal{L}_{total,1}$  and  $\mathcal{L}_{total,2}$ , respectively.
- 6:   **if**  $e > E_A$  **then**
- 7:     Fix  $G_1, G_2, w, \beta$ . Update  $\alpha$  and  $\gamma$  of  $f(\theta_1)$  and  $f(\theta_2)$  by minimizing  $\mathcal{L}_{total,1}$  and  $\mathcal{L}_{total,2}$ , respectively.
- 8:   **end if**
- 9: **end for**

**4 EXPERIMENTS****4.1 Datasets**

To evaluate the effectiveness of our proposed HCS-TNAS method, three public datasets are utilized: (i) **CAMUS dataset** [15] is a large-scale 2D echocardiography dataset, comprising 2000 labeled images, and approximately 19000 unlabeled images. It includes four classes of labels: left ventricle endocardium (LV), left atrium, myocardium, and background. (ii) **HMC-QU dataset** [14] consists of 2D echocardiography videos. By splitting these sequences into individual images, a total of 4989 images are obtained, among which 2349 images are annotated with two classes of labels: left ventricle wall and background. (iii) **CETUS dataset** [4] comprises 90 sequences of 3D ultrasound volumes. After randomly selecting 80 frames from each sequence, a total of 7200 annotated images are obtained, with two classes of labels: LV and background. In our experiments, 3400 of these images are utilized as unlabeled data.

For the CAMUS dataset, the training and test sets comprise 1800 and 200 labeled images, respectively, while for the CETUS dataset, they comprise 3400 and 400 labeled images, and for the HMC-QU dataset, they comprise 2000 and 349 labeled images. For the SSL experiments with HCS-TNAS on the CAMUS dataset, we randomly selected 90, 270, 450, and 900 images from the training set,

corresponding to 5%, 15%, 25%, and 50% labeled data, respectively, while using 19432 unlabeled images for training. On the CETUS dataset, we randomly selected 170, 510, 850, and 1700 images from the training set, corresponding to 5%, 15%, 25%, and 50% labeled data, respectively, and used 3400 unlabeled images for training. For the HMC-QU dataset, 100, 300, 500, and 1000 images are randomly selected as 5%, 15%, 25%, and 50% labeled data, respectively, while 2640 unlabeled images are used for training.

**4.2 Implementation Details**

**4.2.1 Network Architecture.** In the encoder NAS, each cell has  $N = 5$  intermediate nodes. For the resolution  $r = 4$ , the channel numbers are fixed as 8 for each node. When  $r$  doubles, the number of channels doubles accordingly. For partial channel connections,  $\frac{1}{4}$  of the channels are allowed for searching. The default number of layers  $L$  is set to 8 and the default proportion of labeled data utilized is 50%.

**4.2.2 Training Setup.** The experiments are conducted using PyTorch on an Nvidia RTX 3090Ti GPU. The hyper-parameters  $\lambda_1 = 1$ ,  $\lambda_2 = \lambda_4 = 5 \exp(-5(1 - \frac{\min(i, I_{ramp})}{I_{ramp}})^2)$  are adopted following [11, 34] at the  $i^{th}$  epoch, where  $I_{ramp} = 50$ , and  $\lambda_3 = 2$ . The impact of the hyper-parameters is discussed in Sec. 4.5. The linear coefficient matrices  $G$  are optimized by Adam [13] with a fixed learning rate of 0.001. The network weights  $w$  and architecture parameters  $\beta$  are optimized using SGD with an initial learning rate of 0.001, a momentum of 0.9, and a weight decay of 0.0003. For the architecture parameters  $\alpha$  and  $\gamma$ , the Adam optimizer is applied with a learning rate of 0.003 and weight decay of 0.001. The total number of epochs is set to  $E = 40$  and the architecture optimization begins at  $E_A = 10$ . In each epoch,  $G$  is updated  $E_B = 6$  times.

**4.2.3 Metrics.** Three measures are used for evaluation: the Dice Similarity Coefficient (DSC), the Intersection over Union (IoU), and the 95% Hausdorff Distance (95HD). The experiments are repeated with 5 different random seeds, and the average accuracy and standard deviation are reported, with the standard deviations shown in parentheses. The best results are highlighted in **bold**.

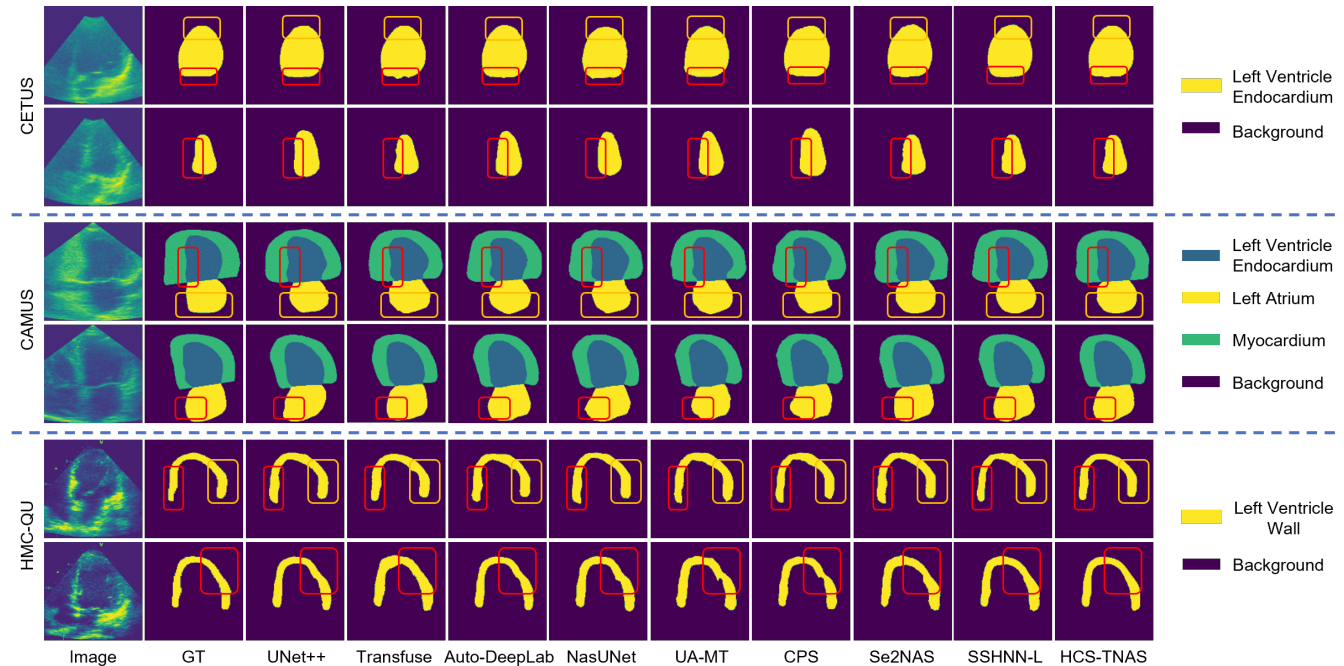


Figure 4: Visualization of segmentation results obtained by our proposed HCS-TNAS and other SOTA methods on the CETUS, CAMUS, and HMC-QU datasets. Note that Resize and crop operations are applied to the model’s predictions to visualize their segmentation differences. Red or orange boxes are used to highlight key regions, demonstrating that our method mitigates both over-segmentation and under-segmentation issues, yielding segmented shapes that closely match expert annotations.

Table 4: Ablation studies of each component in the proposed network structure on CAMUS, HMC-QU, and CETUS datasets.

No.	Efficient NAS-ViT	$\mathcal{L}_{uns}$	$\mathcal{L}_{ind}$	$\mathcal{L}_{con}$	HMC-QU (50%)			CETUS (50%)			CAMUS (50%)		
					DSC $\uparrow$	IoU $\uparrow$	95HD $\downarrow$	DSC $\uparrow$	IoU $\uparrow$	95HD $\downarrow$	DSC $\uparrow$	IoU $\uparrow$	95HD $\downarrow$
1	✗	✗	✗	✗	0.905 <sub>(0.002)</sub>	0.906 <sub>(0.003)</sub>	4.310 <sub>(0.204)</sub>	0.951 <sub>(0.005)</sub>	0.967 <sub>(0.004)</sub>	2.357 <sub>(0.196)</sub>	0.918 <sub>(0.003)</sub>	0.854 <sub>(0.003)</sub>	6.587 <sub>(0.440)</sub>
2	✓	✗	✗	✗	0.912 <sub>(0.001)</sub>	0.911 <sub>(0.002)</sub>	3.623 <sub>(0.131)</sub>	0.959 <sub>(0.002)</sub>	0.969 <sub>(0.002)</sub>	2.049 <sub>(0.099)</sub>	0.924 <sub>(0.004)</sub>	0.860 <sub>(0.007)</sub>	5.924 <sub>(0.566)</sub>
3	✗	✓	✗	✗	0.910 <sub>(0.001)</sub>	0.910 <sub>(0.001)</sub>	3.674 <sub>(0.100)</sub>	0.959 <sub>(0.002)</sub>	0.970 <sub>(0.001)</sub>	2.064 <sub>(0.103)</sub>	0.923 <sub>(0.002)</sub>	0.860 <sub>(0.003)</sub>	6.024 <sub>(0.313)</sub>
4	✗	✓	✓	✗	0.919 <sub>(0.001)</sub>	0.920 <sub>(0.002)</sub>	3.058 <sub>(0.093)</sub>	0.962 <sub>(0.001)</sub>	0.974 <sub>(0.001)</sub>	1.926 <sub>(0.051)</sub>	0.930 <sub>(0.003)</sub>	0.871 <sub>(0.004)</sub>	5.329 <sub>(0.277)</sub>
5	✗	✓	✗	✓	0.917 <sub>(0.003)</sub>	0.915 <sub>(0.002)</sub>	3.356 <sub>(0.297)</sub>	0.960 <sub>(0.003)</sub>	0.971 <sub>(0.002)</sub>	2.011 <sub>(0.148)</sub>	0.927 <sub>(0.005)</sub>	0.864 <sub>(0.006)</sub>	5.509 <sub>(0.501)</sub>
6	✓	✓	✗	✗	0.919 <sub>(0.002)</sub>	0.918 <sub>(0.002)</sub>	3.041 <sub>(0.165)</sub>	0.963 <sub>(0.002)</sub>	0.975 <sub>(0.002)</sub>	1.903 <sub>(0.115)</sub>	0.929 <sub>(0.002)</sub>	0.869 <sub>(0.002)</sub>	5.395 <sub>(0.264)</sub>
7	✓	✓	✓	✗	0.926 <sub>(0.002)</sub>	0.925 <sub>(0.001)</sub>	2.752 <sub>(0.102)</sub>	0.968 <sub>(0.001)</sub>	0.977 <sub>(0.001)</sub>	1.788 <sub>(0.047)</sub>	0.934 <sub>(0.001)</sub>	0.879 <sub>(0.002)</sub>	5.205 <sub>(0.189)</sub>
8	✓	✓	✓	✓	0.933 <sub>(0.002)</sub>	0.931 <sub>(0.002)</sub>	2.480 <sub>(0.161)</sub>	0.972 <sub>(0.001)</sub>	0.978 <sub>(0.001)</sub>	1.620 <sub>(0.036)</sub>	0.937 <sub>(0.002)</sub>	0.884 <sub>(0.003)</sub>	5.042 <sub>(0.168)</sub>

### 4.3 Comparison with SOTA Methods

Table 3 presents the quantitative results of various methods on the HMC-QU, CETUS, and CAMUS datasets. SSL methods are trained using 50% of annotated data, while supervised learning methods are trained using 100% of annotated data without utilizing any unlabeled data. The mainstream segmentation methods are classified based on the learning paradigm and design strategy. Representative works from each group are selected for a comprehensive analysis. It can be observed that HCS-TNAS achieves the best results across all evaluation metrics. On the HMC-QU dataset, HCS-TNAS outperforms the original SOTA method (SSHNN-L) by approximately 2.0% in DSC, 1.9% in IoU, and 1.131 in 95HD, while it also achieves superior performance on the CAMUS and CETUS datasets. These

results demonstrate that our proposed method offers an effective solution to two main issues in ultrasound image segmentation.

Fig. 4 elaborates the qualitative results of various methods. It can be observed that our method mitigates over and under-segmentation issues, and exhibits smoother boundaries between different labels.

### 4.4 Ablation Studies

**4.4.1 Effects of Sub-modules.** To analyze the effects of each sub-module, experiments are conducted in Table 4. The baseline model (No. 1) is the NAS backbone (Sec 3.3) without the Efficient NAS-ViT module, trained using 50% of the annotated data. Firstly, incorporating the Efficient NAS-ViT module improves the segmentation performance from a DSC of 0.905 to 0.912 on the HMC-QU dataset, consistent with the expectation of enhancing the context extraction

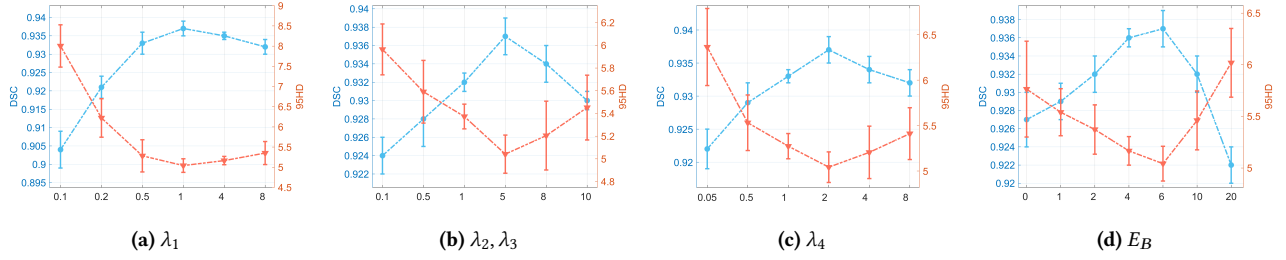


**Figure 5: Ablation experiments on different hyper-parameters. (a) Supervised loss coefficient  $\lambda_1$ . (b) Unsupervised loss coefficient  $\lambda_2$  and network independence loss coefficient  $\lambda_3$ . (c) Contrastive loss coefficient  $\lambda_4$ . (d) Beta epochs  $E_B$ , which denotes the level of emphasis placed on algorithmic independence.**

**Table 5: Discussion of different Transformer application modes on the HMC-QU dataset.**

Type	Method	Application Mode	DSC $\uparrow$	IoU $\uparrow$	95HD $\downarrow$	Params (M) $\downarrow$	FLOPs (G) $\downarrow$
Manual	TransUNet [6]	Employ Transformer as Encoder	0.906 <sub>(0.003)</sub>	0.905 <sub>(0.004)</sub>	4.032 <sub>(0.207)</sub>	96.07	<b>48.34</b>
Manual	EfficientViT-L2 [5]	Multi-scale Tokens	0.916 <sub>(0.005)</sub>	0.915 <sub>(0.004)</sub>	3.356 <sub>(0.260)</sub>	52.12	91.45
NAS	Auto-DeepLab [16]	No Transformer is Applied	0.908 <sub>(0.004)</sub>	0.907 <sub>(0.004)</sub>	3.857 <sub>(0.164)</sub>	44.42	347.52
NAS	SSHNN-L [7]	Treat Transformer as Additional Branch	0.913 <sub>(0.002)</sub>	0.912 <sub>(0.002)</sub>	3.611 <sub>(0.145)</sub>	<b>38.82</b>	52.78
NAS	DAST [32]	Treat Transformer as Candidate Operation	0.915 <sub>(0.002)</sub>	0.913 <sub>(0.002)</sub>	3.438 <sub>(0.119)</sub>	192.44	110.36
NAS	<b>HCS-TNAS-E</b>	Treat EfficientViT as Candidate Operation	0.923 <sub>(0.001)</sub>	0.922 <sub>(0.002)</sub>	2.884 <sub>(0.123)</sub>	<b>38.48</b>	55.47
NAS	<b>HCS-TNAS</b>	Efficient NAS-ViT	<b>0.933<sub>(0.002)</sub></b>	<b>0.931<sub>(0.002)</sub></b>	<b>2.480<sub>(0.161)</sub></b>	41.20	67.50

capabilities. After introducing the co-training algorithm as the SSL framework (No. 6), HCS-TNAS obtains 0.7%, 0.4%, and 0.5% DSC improvements on three datasets, respectively, attributed to the additional information gained from the unlabeled data facilitated by the SSL. Furthermore, when the network independence loss is considered (No. 7), there are 17.12%, 7.66%, and 15.53% 95HD increments over the previous version (No. 6) on three datasets respectively. The effectiveness of contrastive learning is validated in No. 5, which improves the performance by 0.77% in DSC on the HMC-QU dataset compared to independently using the  $\mathcal{L}_{uns}$  in No. 3.

**4.4.2 Effects of Transformer Application Modes.** Table 5 presents an assessment of various networks employing different Transformer application modes. TransUNet uses pure Transformers as the encoder. EfficientViT-L2 uses fixed multi-scale tokens within the Transformer. Auto-DeepLab is a NAS model that does not apply the Transformer. SSHNN-L is a NAS network that adopts Transformers as an additional branch. DAST directly uses the Transformer as a candidate operation during the network search process. In the HCS-TNAS-E, we also evaluated the case where EfficientViT was treated as a candidate operation instead of employing the Efficient NAS-ViT. While maintaining the highest segmentation accuracy, our method exhibits a smaller model scale and lower FLOPs. Moreover, the results of the HCS-TNAS-E variant clearly show that the Transformer application mode significantly impacts model performance.

**4.4.3 Impact of the Annotation Ratio.** Table 6 elaborates the results of representative SSL networks and HCS-TNAS with varying proportions of annotations. It can be observed that HCS-TNAS performs more stable than other advanced SSL methods. When the annotation ratio descends from 50% to 5%, the DSC of UA-MT,

CPS, Se<sup>2</sup>NAS, and SSHNN-L drops by 13.6%, 14.4%, 6.6%, and 6.9%, respectively. However, the DSC of HCS-TNAS only decreases by 4.6%, verifying its robustness. We attribute this achievement to the hybrid constraint-driven SSL approach, which enhances the utilization of limited data.

**4.4.4 Sensitivity Analysis of Hybrid Constraints.** We investigate whether excluding the algorithmic independence loss  $\mathcal{L}_{ind}$  or contrastive loss  $\mathcal{L}_{con}$  would impact its performance under varying annotation ratios, presented in Table 7. When both  $\mathcal{L}_{ind}$  and  $\mathcal{L}_{con}$  are removed, there is a 3.4% drop in DSC as the annotation ratio decreases from 50% to 25%, which is larger than the 2.7% and 2.8% DSC decreases observed when  $\mathcal{L}_{con}$  or  $\mathcal{L}_{ind}$  is excluded, respectively. Notably, the DSC of HCS-TNAS decreases by 1.7%, representing the smallest drop among these cases. These results align with our expectations as  $\mathcal{L}_{ind}$  encourages the creation of complementary networks that assist in training by providing multi-view information from the same data, especially when focusing on the convolution layers responsible for feature extraction and aggregation. Additionally, as for  $\mathcal{L}_{con}$ , by considering feature-level uncertainty in SSL, the enhanced underlying structural information between the locally aware CNN and the globally aware Transformer is facilitated. Specifically, regions with lower uncertainty are filtered out, which contributes to stable training under limited annotations.

## 4.5 Study on Hyper-parameter Sensitivity

The sensitivity of our method to different hyper-parameter settings under a 50% annotation ratio is illustrated in Fig. 5. As shown in Fig. 5(a), the fluctuations in DSC caused by varying  $\lambda_1$  indicate that the supervised loss plays a dominant role. From Fig. 5(b), we observe that assigning a low weight to the initial value of  $\lambda_2$  weakens the



**Table 6: Ablation Studies of different annotation proportions on the CAMUS dataset.**

Method	CAMUS (5%)			CAMUS (15%)			CAMUS (25%)			CAMUS (50%)		
	DSC↑	IoU↑	95HD↓	DSC↑	IoU↑	95HD↓	DSC↑	IoU↑	95HD↓	DSC↑	IoU↑	95HD↓
UA-MT	0.772 <sub>(0.003)</sub>	0.706 <sub>(0.005)</sub>	20.951 <sub>(0.529)</sub>	0.849 <sub>(0.004)</sub>	0.754 <sub>(0.005)</sub>	12.617 <sub>(0.546)</sub>	0.892 <sub>(0.004)</sub>	0.814 <sub>(0.005)</sub>	8.486 <sub>(0.478)</sub>	0.908 <sub>(0.002)</sub>	0.837 <sub>(0.002)</sub>	7.440 <sub>(0.161)</sub>
CPS	0.757 <sub>(0.002)</sub>	0.683 <sub>(0.003)</sub>	22.879 <sub>(0.342)</sub>	0.843 <sub>(0.003)</sub>	0.742 <sub>(0.005)</sub>	13.322 <sub>(0.502)</sub>	0.890 <sub>(0.005)</sub>	0.810 <sub>(0.007)</sub>	8.706 <sub>(0.697)</sub>	0.901 <sub>(0.004)</sub>	0.827 <sub>(0.005)</sub>	8.864 <sub>(0.477)</sub>
Se <sup>2</sup> NAS	0.854 <sub>(0.004)</sub>	0.764 <sub>(0.005)</sub>	11.855 <sub>(0.710)</sub>	0.882 <sub>(0.002)</sub>	0.800 <sub>(0.004)</sub>	9.295 <sub>(0.485)</sub>	0.906 <sub>(0.003)</sub>	0.831 <sub>(0.003)</sub>	7.831 <sub>(0.302)</sub>	0.920 <sub>(0.002)</sub>	0.856 <sub>(0.003)</sub>	6.410 <sub>(0.311)</sub>
SSHNN-L	0.860 <sub>(0.005)</sub>	0.773 <sub>(0.005)</sub>	11.012 <sub>(0.676)</sub>	0.894 <sub>(0.004)</sub>	0.814 <sub>(0.006)</sub>	8.511 <sub>(0.576)</sub>	0.908 <sub>(0.001)</sub>	0.835 <sub>(0.003)</sub>	7.331 <sub>(0.299)</sub>	0.929 <sub>(0.002)</sub>	0.868 <sub>(0.003)</sub>	5.516 <sub>(0.278)</sub>
<b>HCS-TNAS</b>	<b>0.891<sub>(0.003)</sub></b>	<b>0.810<sub>(0.004)</sub></b>	<b>8.604<sub>(0.365)</sub></b>	<b>0.911<sub>(0.002)</sub></b>	<b>0.841<sub>(0.002)</sub></b>	<b>6.711<sub>(0.435)</sub></b>	<b>0.919<sub>(0.001)</sub></b>	<b>0.854<sub>(0.002)</sub></b>	<b>6.591<sub>(0.332)</sub></b>	<b>0.937<sub>(0.002)</sub></b>	<b>0.884<sub>(0.003)</sub></b>	<b>5.042<sub>(0.168)</sub></b>

**Table 7: Sensitivity analysis of hybrid constraints.**

Method	HMC-QU (25%)		HMC-QU (50%)	
	DSC↑	95HD↓	DSC↑	95HD↓
Remove $\mathcal{L}_{ind}, \mathcal{L}_{con}$	0.885 <sub>(0.005)</sub>	6.468 <sub>(0.283)</sub>	0.919 <sub>(0.002)</sub>	3.041 <sub>(0.165)</sub>
Remove $\mathcal{L}_{con}$	0.899 <sub>(0.003)</sub>	4.855 <sub>(0.217)</sub>	0.926 <sub>(0.002)</sub>	2.752 <sub>(0.102)</sub>
Remove $\mathcal{L}_{ind}$	0.893 <sub>(0.004)</sub>	5.229 <sub>(0.265)</sub>	0.921 <sub>(0.003)</sub>	2.934 <sub>(0.184)</sub>
<b>HCS-TNAS</b>	<b>0.916<sub>(0.004)</sub></b>	<b>3.526<sub>(0.171)</sub></b>	<b>0.933<sub>(0.002)</sub></b>	<b>2.480<sub>(0.161)</sub></b>

role of the co-training while setting it too high causes HCS-TNAS to deviate from the main segmentation task. This principle is also applicable to the contrastive loss coefficient  $\lambda_3$ . As observed in Fig. 5(c) and (d), the degree of emphasis on network independence has an obvious influence. When  $\lambda_4 = 2$  and  $E_B = 6$ , we obtain the highest DSC, whereas assigning a small weight to the independence loss fails to utilize the advantage of co-training, and a small number of iterations also lead to insufficient network independence estimation. On the other hand, an excessive focus on independence causes the NAS backbone to deviate from the optimum.

## 5 CONCLUSION

In this paper, we propose a hybrid constraint-driven semi-supervised Transformer-NAS (HCS-TNAS) to address two key challenges in ultrasound segmentation: enhance multi-scale feature understanding and mitigate data dependency. For the first issue, HCS-TNAS implements a three-level search strategy, coupled with an Efficient NAS-ViT module designed to enhance contextual feature extraction. For the second issue, we propose a hybrid constraint-driven SSL framework to boost model performance under limited annotations. Extensive experiments on three public datasets prove the effectiveness of the proposed method.

## REFERENCES

- [1] Yasser Ali, Farrokh Janabi-Sharifi, and Soosan Beheshti. 2021. Echocardiographic image segmentation using deep Res-U network. *Biomedical Signal Processing and Control* 64 (2021), 102248.
- [2] Philip Bachman, R Devon Hjelm, and William Buchwalter. 2019. Learning representations by maximizing mutual information across views. *Advances in neural information processing systems* 32 (2019).
- [3] Wenjia Bai, Ozan Oktay, Matthew Sinclair, Hideaki Suzuki, Martin Rajchl, Giacomo Tarroni, Ben Glocker, Andrew King, Paul M Matthews, and Daniel Rueckert. 2017. Semi-supervised learning for network-based cardiac MR image segmentation. In *Medical Image Computing and Computer-Assisted Intervention- MICCAI 2017: 20th International Conference, Quebec City, QC, Canada, September 11-13, 2017, Proceedings, Part II* 20. Springer, 253–260.
- [4] Olivier Bernard, Johan G Bosch, Brecht Heyde, Martino Alessandrini, Daniel Barbosa, Sorina Camarasu-Pop, Frederic Cervenansky, Sébastien Valette, Oana Mirea, Michel Bernier, et al. 2015. Standardized evaluation system for left ventricular segmentation algorithms in 3D echocardiography. *IEEE transactions on medical imaging* 35, 4 (2015), 967–977.
- [5] Han Cai, Junyan Li, Muyan Hu, Chuang Gan, and Song Han. 2023. Efficientvit: Lightweight multi-scale attention for high-resolution dense prediction. In *Proceedings of the IEEE/CVF International Conference on Computer Vision*. 17302–17313.
- [6] Jeneng Chen, Yongyi Lu, Qihang Yu, Xiangde Luo, Ehsan Adeli, Yan Wang, Le Lu, Alan L Yuille, and Yuyin Zhou. 2021. Transunet: Transformers make strong encoders for medical image segmentation. *arXiv preprint arXiv:2102.04306* (2021).
- [7] Renqi Chen, Jingjing Luo, Fan Nian, Yuhui Cen, Yiheng Peng, and Zekuan Yu. 2024. SSHNN: Semi-Supervised Hybrid NAS Network for Echocardiographic Image Segmentation. In *ICASSP 2024-2024 IEEE International Conference on Acoustics, Speech and Signal Processing (ICASSP)*. IEEE, 1541–1545.
- [8] Xiaokang Chen, Yuhui Yuan, Gang Zeng, and Jingdong Wang. 2021. Semi-supervised semantic segmentation with cross pseudo supervision. In *Proceedings of the IEEE/CVF Conference on Computer Vision and Pattern Recognition*. 2613–2622.
- [9] Alexey Dosovitskiy, Lucas Beyer, Alexander Kolesnikov, Dirk Weissenborn, Xiuhua Zhai, Thomas Unterthiner, Mostafa Dehghani, Matthias Minderer, Georg Heigold, Sylvain Gelly, et al. 2020. An image is worth 16x16 words: Transformers for image recognition at scale. *arXiv preprint arXiv:2010.11929* (2020).
- [10] Kaiming He, Xiangyu Zhang, Shaoqing Ren, and Jian Sun. 2016. Deep residual learning for image recognition. In *Proceedings of the IEEE conference on computer vision and pattern recognition*. 770–778.
- [11] Huimin Huang, Yawen Huang, Shiao Xie, Lanfen Lin, Tong Ruofeng, Yen-wei Chen, Yuexiang Li, and Yefeng Zheng. 2023. Semi-Supervised Convolutional Vision Transformer with Bi-Level Uncertainty Estimation for Medical Image Segmentation. In *Proceedings of the 31st ACM International Conference on Multimedia*. 5214–5222.
- [12] Fabian Isensee, Paul F Jaeger, Simon AA Kohl, Jens Petersen, and Klaus H Maier-Hein. 2021. nnU-Net: a self-configuring method for deep learning-based biomedical image segmentation. *Nature methods* 18, 2 (2021), 203–211.
- [13] Diederik P Kingma and Jimmy Ba. 2014. Adam: A method for stochastic optimization. *arXiv preprint arXiv:1412.6980* (2014).
- [14] Serkan Kiranyaz, Aysen Degerli, Tahir Hamid, Rashid Mazhar, Rayyan El Fadil Ahmed, Raya Abouhasera, Morteza Zabih, Junaid Malik, Ridha Hamila, and Moncef Gabbouj. 2020. Left ventricular wall motion estimation by active polynomials for acute myocardial infarction detection. *IEEE Access* 8 (2020), 210301–210317.
- [15] Sarah Leclerc, Erik Smistad, Joao Pedrosa, Andreas Østvik, Frederic Cervenansky, Florian Espinosa, Torvald Espeland, Erik Andreas Rye Berg, Pierre-Marc Jodoin, Thomas Grenier, et al. 2019. Deep learning for segmentation using an open large-scale dataset in 2D echocardiography. *IEEE transactions on medical imaging* 38, 9 (2019), 2198–2210.
- [16] Chenxi Liu, Liang-Chieh Chen, Florian Schroff, Hartwig Adam, Wei Hua, Alan L Yuille, and Li Fei-Fei. 2019. Auto-deeplab: Hierarchical neural architecture search for semantic image segmentation. In *Proceedings of the IEEE/CVF conference on computer vision and pattern recognition*. 82–92.

- [17] Hanxiao Liu, Karen Simonyan, and Yiming Yang. 2018. Darts: Differentiable architecture search. *arXiv preprint arXiv:1806.09055* (2018).
- [18] Zexin Lu, Wenjun Xia, Yongqiang Huang, Mingzheng Hou, Hu Chen, Jiliu Zhou, Hongming Shan, and Yi Zhang. 2022. M 3 NAS: Multi-scale and multi-level memory-efficient neural architecture search for low-dose CT denoising. *IEEE Transactions on Medical Imaging* 42, 3 (2022), 850–863.
- [19] Xiangde Luo, Wenjun Liao, Jieneng Chen, Tao Song, Yinan Chen, Shichuan Zhang, Nianyong Chen, Guotai Wang, and Shaoting Zhang. 2021. Efficient semi-supervised gross target volume of nasopharyngeal carcinoma segmentation via uncertainty rectified pyramid consistency. In *Medical Image Computing and Computer Assisted Intervention—MICCAI 2021: 24th International Conference, Strasbourg, France, September 27–October 1, 2021, Proceedings, Part II* 24. Springer, 318–329.
- [20] Juzheng Miao, Cheng Chen, Furui Liu, Hao Wei, and Pheng-Ann Heng. 2023. CauSSL: Causality-inspired Semi-supervised Learning for Medical Image Segmentation. In *Proceedings of the IEEE/CVF International Conference on Computer Vision*. 21426–21437.
- [21] Loïc Pauleto, Massih-Reza Amini, and Nicolas Winckler. 2022. Se 2 NAS: Self-Semi-Supervised architecture optimization for Semantic Segmentation. In *2022 26th International Conference on Pattern Recognition (ICPR)*. IEEE, 54–60.
- [22] Siyuan Qiao, Wei Shen, Zhishuai Zhang, Bo Wang, and Alan Yuille. 2018. Deep co-training for semi-supervised image recognition. In *Proceedings of the european conference on computer vision (eccv)*. 135–152.
- [23] Shenghan Ren, Yongbing Wang, Rui Hu, Lei Zuo, Liwen Liu, and Heng Zhao. 2021. Automated segmentation of left ventricular myocardium using cascading convolutional neural networks based on echocardiography. *AIP Advances* 11, 4 (2021).
- [24] Olaf Ronneberger, Philipp Fischer, and Thomas Brox. 2015. U-net: Convolutional networks for biomedical image segmentation. In *Medical Image Computing and Computer-Assisted Intervention—MICCAI 2015: 18th International Conference, Munich, Germany, October 5–9, 2015, Proceedings, Part III* 18. Springer, 234–241.
- [25] Ning Shen, Tingfa Xu, Ziyang Bian, Shiqi Huang, Feng Mu, Bo Huang, Yuze Xiao, and Jianan Li. 2022. SCANet: A unified semi-supervised learning framework for vessel segmentation. *IEEE Transactions on Medical Imaging* (2022).
- [26] Antti Tarvainen and Harri Valpola. 2017. Mean teachers are better role models: Weight-averaged consistency targets improve semi-supervised deep learning results. *Advances in neural information processing systems* 30 (2017).
- [27] Guotai Wang, Shuwei Zhai, Giovanni Lasio, Baoshe Zhang, Byong Yi, Shifeng Chen, Thomas J Macvittie, Dimitris Metaxas, Jinghao Zhou, and Shaoting Zhang. 2021. Semi-supervised segmentation of radiation-induced pulmonary fibrosis from lung CT scans with multi-scale guided dense attention. *IEEE transactions on medical imaging* 41, 3 (2021), 531–542.
- [28] Yu Weng, Tianbao Zhou, Yujie Li, and Xiaoyu Qiu. 2019. Nas-unet: Neural architecture search for medical image segmentation. *IEEE access* 7 (2019), 44247–44257.
- [29] Huisi Wu, Jiasheng Liu, Fangyan Xiao, Zhenkun Wen, Lan Cheng, and Jing Qin. 2022. Semi-supervised segmentation of echocardiography videos via noise-resilient spatiotemporal semantic calibration and fusion. *Medical Image Analysis* 78 (2022), 102397.
- [30] Yingda Xia, Dong Yang, Zhiding Yu, Fengze Liu, Jinzheng Cai, Lequan Yu, Zhuotun Zhu, Daguang Xu, Alan Yuille, and Holger Roth. 2020. Uncertainty-aware multi-view co-training for semi-supervised medical image segmentation and domain adaptation. *Medical image analysis* 65 (2020), 101766.
- [31] Yuhui Xu, Lingxi Xie, Xiaopeng Zhang, Xin Chen, Guo-Jun Qi, Qi Tian, and Hongkai Xiong. 2019. Pc-darts: Partial channel connections for memory-efficient architecture search. *arXiv preprint arXiv:1907.05737* (2019).
- [32] Dong Yang, Ziyue Xu, Yufan He, Vishwesh Nath, Wenqi Li, Andriy Myronenko, Ali Hatamizadeh, Can Zhao, Holger R Roth, and Daguang Xu. 2023. DAST: Differentiable Architecture Search with Transformer for 3D Medical Image Segmentation. In *International Conference on Medical Image Computing and Computer-Assisted Intervention*. Springer, 747–756.
- [33] Li Yu, Yi Guo, Yuanyuan Wang, Jinhua Yu, and Ping Chen. 2016. Segmentation of fetal left ventricle in echocardiographic sequences based on dynamic convolutional neural networks. *IEEE Transactions on Biomedical Engineering* 64, 8 (2016), 1886–1895.
- [34] Lequan Yu, Shujun Wang, Xiaomeng Li, Chi-Wing Fu, and Pheng-Ann Heng. 2019. Uncertainty-aware self-ensembling model for semi-supervised 3D left atrium segmentation. In *Medical Image Computing and Computer Assisted Intervention—MICCAI 2019: 22nd International Conference, Shenzhen, China, October 13–17, 2019, Proceedings, Part II* 22. Springer, 605–613.
- [35] Zhihong Yu, Feifei Lee, and Qiu Chen. 2023. HCT-net: hybrid CNN-transformer model based on a neural architecture search network for medical image segmentation. *Applied Intelligence* (2023), 1–17.
- [36] Xiong Zhang, Hongmin Xu, Hong Mo, Jianchao Tan, Cheng Yang, Lei Wang, and Wenqi Ren. 2021. Denas: Densely connected neural architecture search for semantic image segmentation. In *Proceedings of the IEEE/CVF conference on computer vision and pattern recognition*. 13956–13967.
- [37] Yundong Zhang, Huiye Liu, and Qiang Hu. 2021. Transfuse: Fusing transformers and cnns for medical image segmentation. In *Medical Image Computing and Computer Assisted Intervention—MICCAI 2021: 24th International Conference, Strasbourg, France, September 27–October 1, 2021, Proceedings, Part I* 24. Springer, 14–24.
- [38] Guang-Quan Zhou, Wen-Bo Zhang, Zhong-Qing Shi, Zhan-Ru Qi, Kai-Ni Wang, Hong Song, Jing Yao, and Yang Chen. 2023. DSANet: Dual-branch Shape-Aware Network for Echocardiography Segmentation in Apical Views. *IEEE Journal of Biomedical and Health Informatics* (2023).
- [39] Zongwei Zhou, Md Mahfuzur Rahman Siddiquee, Nima Tajbakhsh, and Jianming Liang. 2019. Unet++: Redesigning skip connections to exploit multiscale features in image segmentation. *IEEE transactions on medical imaging* 39, 6 (2019), 1856–1867.

# Supplementary Material

In this supplementary material, we provide additional details and experimental results to enhance the understanding and insights into our proposed HCS-TNAS. This supplementary material is organized as follows:

- A more detailed description of the role of architecture parameters for the NAS backbone in [Sec. 3.3](#) is shown in [Sec. A](#).
- We provide more details about the employed datasets in [Sec. B.1](#) and comprehensive analysis of the experimental results (under the experimental conditions presented in [Sec. B.2](#)) from the perspectives of training convergence, statistical significance testing, and proportions of candidate operations in [Sec. B.3, B.4, and B.5](#), respectively.
- We present additional ablation studies in [Sec. C.1](#), and [C.2](#), analyzing the effects of various candidate operation sets and different feature resolutions used in the contrastive loss, respectively.
- We also present additional parameter studies in [Sec. D](#), discussing the impact of the network size.
- Finally, we discuss the potential limitations of the proposed HCS-TNAS and future research directions in [Sec. E](#).

**Table 8: Cell candidate operations.**

Candidate Operations	Encoder Cell	Decoder Cell
3×3 separable convolution	✓	✓
5×5 separable convolution	✓	✓
3×3 convolution with dilation rate 2	✓	✓
5×5 convolution with dilation rate 2	✓	✓
3×3 average/max pooling	✓	✗
skip connection	✓	✓
no connection (zero)	✓	✗

## A MORE DETAILS ABOUT HCS-TNAS

As we introduced in [Sec. 3.3](#) of the main paper, the architecture parameters  $\alpha$  and  $\gamma$  are responsible for updating the candidate operations in the encoder and decoder cells, respectively. In HCS-TNAS, to enlarge the search space, unlike existing works where all cells share the same architecture parameters, our architecture parameters  $\alpha$  are defined as a 3-dimensional tuple (*Cell, Edge, Operation*), and  $\gamma$  is defined as a 2-dimensional tuple (*Cell, Operation*).

- *Cell* indicates that different cells are optimized by specialized parameters, overcoming the limitation of a simple cell type, and enabling a larger search space to be explored.
- *Edge* represents the connection between each intermediate node within a cell, which is used for feature aggregation at the intermediate nodes. Note that the decoder cell does not have this parameter to reduce the parameter count and training time.
- *Operation* denotes the number of operation types. As shown in [Table 1](#), 8 different choices are provided for the encoder to ensure diversity in the selection, while 5 different choices are

provided for the decoder. The rationale behind designing different candidate operation sets is discussed in [Sec. C.1](#).

Thus, in the search process for the encoder and decoder cells, we allow different cells to have different structures, and different node-to-node connections to have different operations. This approach enables the network to have a vast search space and optimization potential without requiring a large number of layers.

## B MORE EXPERIMENTAL RESULTS

### B.1 Dataset Details

**CAMUS dataset.** The CAMUS dataset [15] is a large open 2D echocardiography dataset collected from 500 patients. Each patient contributes a 4-chamber and a 2-chamber view sequence, each containing approximately 20 unlabeled images. Exceptions are made for annotations at the moments of end-diastole (ED) and end-systole (ES). Thus, there are 2000 labeled images and approximately 19000 unlabeled images. The segmentation labels include four categories: the left ventricle endocardium, the myocardium, the left atrium, and the background. All images are resized to 256×256 pixels for training.

**HMC-QU dataset.** The HMC-QU dataset [14] is composed of 2D echocardiography videos from the apical 4-chamber (A4C) and apical 2-chamber (A2C) views. In a specific subset of HMC-QU dataset, 109 A4C view echocardiography recordings from 72 myocardial infarction (MI) patients and 37 non-MI subjects are annotated for one cardiac cycle. The remaining frames are unlabeled. Through the statistical analysis, the HMC-QU dataset consists of 4989 images in total, with 2349 images labeled for two categories: the left ventricle wall and the background. All images are resized to 192×192 pixels for training.

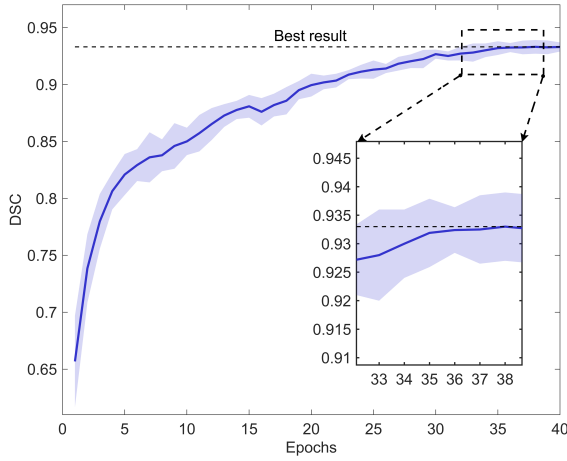
**CETUS dataset.** The CETUS dataset [4] comprises 90 sequences (both ED and ES) of 3D ultrasound volumes capturing one complete cardiac cycle, collected from 45 patients. It can be categorized into three subgroups: 15 healthy individuals, 15 patients with a history of myocardial infarction at least 3 months prior to data acquisition, and 15 patients with dilated cardiomyopathy. To address the non-uniform duration of left ventricle endocardium presence and ensure fairness, we randomly selected 80 frames from each sequence to form the dataset. Consequently, the selection process provides 7200 labeled images, all resized to 192×192 pixels. The ground-truth mask consists of two distinct labels: the left ventricle endocardium and the background.

### B.2 Implementation Details

**Network Architecture.** In the encoder NAS, each cell has  $N = 5$  intermediate nodes. For the resolution  $r = 4$ , the channel numbers  $C$  are fixed as 8 for each node. When  $r$  doubles, the number of channels doubles accordingly. For partial channel connections,  $\frac{1}{4}$  of the channels are allowed for searching, following the settings in [31]. The default number of layers  $L$  is set to 8 and the default proportion of labeled data utilized is 50%.

**Table 9: Tests for statistical significance (*t*-Test) of Dice.** ◦ represents the statistical difference between HCS-TNAS and other methods. (◦ :  $p \leq 0.05$ , ◦◦ :  $p \leq 0.01$ , ◦◦◦ :  $p \leq 0.001$ )

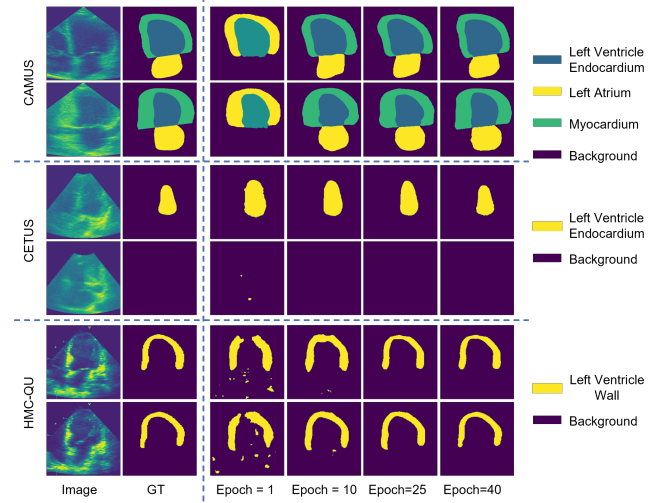
	Fully-supervised						Semi-supervised					HCS-TNAS
	UNet++ [39]	nnU-Net [12]	Transfuse [37]	Auto-DeepLab [16]	M <sup>3</sup> NAS [18]	NasUNet [28]	UA-MT [34]	URPC [19]	CPS [8]	Se <sup>2</sup> NAS [21]	SSHNN-L [7]	
HMC-QU	◦◦◦	◦◦◦	◦◦◦	◦◦◦	◦◦	◦◦◦	◦◦◦	◦◦◦	◦◦◦	◦◦	◦◦	-
CETUS	◦◦◦	◦◦	◦◦	◦◦◦	◦◦	◦◦◦	◦◦◦	◦◦◦	◦◦◦	◦◦◦	◦◦	-
CAMUS	◦◦◦	◦◦	◦◦	◦◦◦	◦◦	◦◦◦	◦◦◦	◦◦◦	◦◦◦	◦◦	◦	-

**Figure 6: Validation accuracy during 40 epochs of architecture search optimization across 10 random trials on the HMC-QU dataset.**

**Training Setup.** The experiments are conducted using PyTorch on an Nvidia RTX 3090Ti GPU. The hyper-parameters  $\lambda_1 = 1$ ,  $\lambda_2 = \lambda_4 = 5 \exp(-5(1 - \frac{\min(i, I_{ramp})}{I_{ramp}})^2)$  are adopted following [11, 34] at the  $i^{th}$  epoch, where  $I_{ramp} = 50$ , and  $\lambda_3 = 2$ . The linear coefficient matrices  $G$  are optimized by Adam [13] with a fixed learning rate of 0.001. The network weights  $w$  and architecture parameters  $\beta$  are optimized using SGD with an initial learning rate of 0.001, a momentum of 0.9, and a weight decay of 0.0003. For the architecture parameters  $\alpha$  and  $\gamma$ , the Adam optimizer is applied with a learning rate of 0.003 and weight decay of 0.001. The total number of epochs is set to  $E = 40$  and the architecture optimization begins at  $E_A = 10$ . In each epoch,  $G$  is updated  $E_B = 6$  times.

### B.3 Convergence Behavior

Fig. 6 depicts the validation accuracy trajectory over 40 epochs during the architecture search optimization process of HCS-TNAS in the metric of DSC, presenting our experimental results across 10 random trials on the HMC-QU dataset using 50% labeled data. While the deep blue curve represents the mean validation accuracy, the light blue shaded region around it suggests variability across trials. The validation accuracy curve exhibits an initial steep ascent, followed by a more gradual increase, ultimately converging

**Figure 7: Qualitative assessment of the segmentation performance of HCS-TNAS throughout the training process. It can be observed that as the number of training iterations increases, the segmentation results gradually approach expert annotations.**

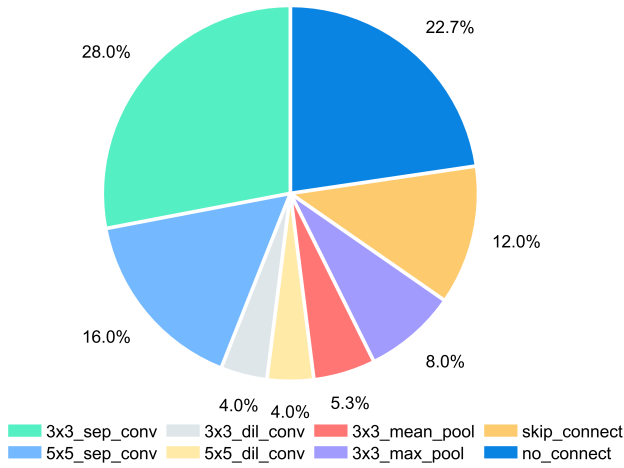
close to 0.933. An inset magnifies the changes of the curve at final epochs, revealing minor fluctuations within a tight range during terminal convergence and presenting stability after 37 epochs. We also experimented with searching for longer epochs (50, 60, 70), but did not observe any significant benefit.

Fig. 7 illustrates the progressive refinement of segmentation predictions during the training process of the HCS-TNAS for ultrasound image segmentation on the CAMUS, CETUS, and HMC-QU datasets, offering an instructive portrayal of the model's progressive enhancement in this clinically significant application.

### B.4 Statistical Significance Test

We conducted a two-tailed paired *t*-test on the DSC scores to analyze the statistical significance between HCS-TNAS and other advanced algorithms, as elaborated in Table 9. For each dataset, we used 200 test samples from the corresponding test sets. A *p*-value less than 0.05 indicates a statistically significant difference between the comparing methods [25]. The circular markers visually underscore the statistically significant improvement of the HCS-TNAS over the compared approaches, indicating its superiority over

the other fully-supervised and semi-supervised techniques by a considerable margin.



**Figure 8: The proportion of each candidate operation in the cells of the encoder NAS of the final searched network on the HMC-QU dataset.**

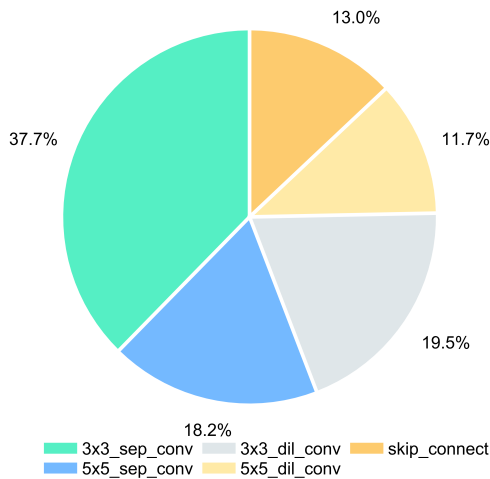


**Figure 9: The proportion of each candidate operation in the cells of the decoder NAS of the final searched network on the HMC-QU dataset.**

## B.5 Analysis on Candidate Operation Proportion

As mentioned previously, we have defined that the cells within both the encoder and decoder architectures possess their distinct architecture parameters rather than sharing them. To gain a deeper insight into the final architecture, the statistical distributions of candidate operations in the final searched encoder and decoder

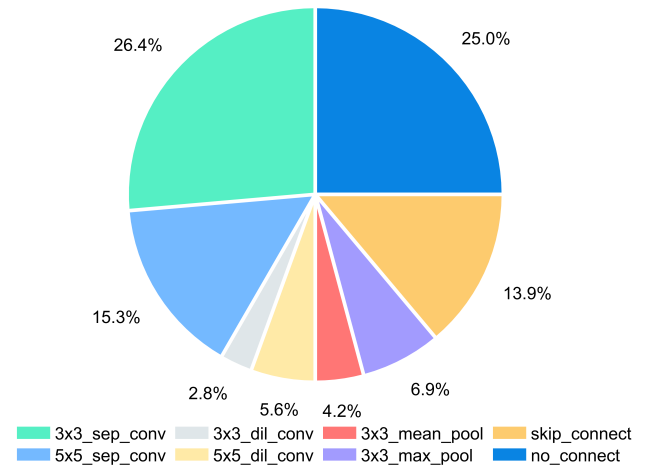


**Figure 10: The proportion of each candidate operation in the cells of the encoder NAS of the final searched network on the CAMUS dataset.**

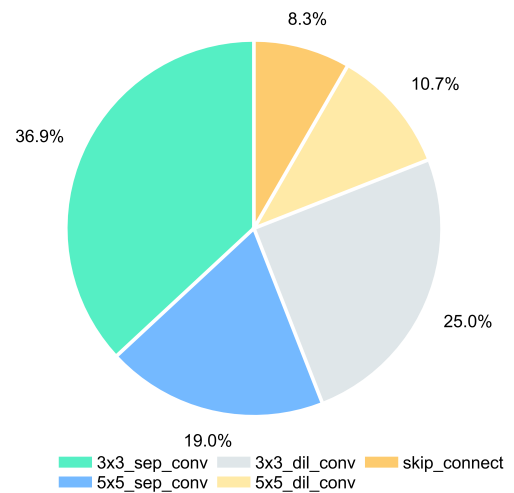


**Figure 11: The proportion of each candidate operation in the cells of the decoder NAS of the final searched network on the CAMUS dataset.**

architecture on three datasets (CAMUS, CETUS, and HMC-QU) are presented in Fig. 8 through Fig. 13, where the compositions of operations within the encoder and decoder cells are individually characterized. The proportion of each candidate operation in the encoder and decoder cells is calculated as follows:

$$P_{O_k \in O^{en}} = \frac{\sum_{i=1}^{\sum Cells} \sum_{j=1}^{\sum Edges} \alpha_{i,j,O_k}}{\sum Cells \sum Edges} \quad (17)$$

and

$$P_{O_k \in O^{de}} = \frac{\sum_{i=1}^{\sum Cells} \alpha_{i,O_k}}{\sum Cells} \quad (18)$$

where  $\sum Cells$  denotes the total number of the encoder or decoder cells, and  $\sum Edges$  denotes the total number of node-to-node edges in the encoder.  $O^{en}$  and  $O^{de}$  represent the sets of candidate operations for the encoder and decoder, respectively.

By comparing the two charts (encoder and decoder) for each dataset, it can be observed that while the decoder favors skip connections and a more diverse set of convolution operations, the encoder places greater emphasis on separable convolutions and also includes pooling operations. Specifically, the decoder architecture searched by NAS has a much higher proportion of dilated convolutions compared to the encoder architecture. This distinction in operation distributions between the decoder and encoder components likely reflects their respective roles and computational requirements within the overall architecture, with the decoder emphasizing skip connections and diverse convolutions for upsampling and feature synthesis, while the encoder focuses on efficient feature extraction through separable convolutions and pooling operations.

## C MORE ABLATION STUDIES

### C.1 Effect of Candidate Operation Set

Table 10 presents an ablation study that investigates the effect of including or excluding pooling and no connection operations from the set of candidate operations for the decoder component, evaluated on the HMC-QU dataset. The differences between the two scenarios are quantified in the final row, demonstrating that excluding pooling and no connection operations from the decoder cells leads to superior performance across all three evaluation metrics.

These empirical findings suggest that, for the given task and dataset, a simpler decoder architecture without pooling and no connection operations is more effective in achieving superior segmentation performance. The inclusion of these operations appears to be detrimental, potentially introducing noise or feature degradation that outweighs any potential benefits.

**Table 10: Ablation study on the set of decoder candidate operations on the HMC-QU dataset.**

Method	DSC $\uparrow$	IoU $\uparrow$	95HD $\downarrow$
Include pooling and no connection	0.924 <sub>(0.005)</sub>	0.923 <sub>(0.004)</sub>	2.961 <sub>(0.238)</sub>
<b>Exclude pooling and no connection</b>	<b>0.933<sub>(0.002)</sub></b>	<b>0.931<sub>(0.002)</sub></b>	<b>2.480<sub>(0.161)</sub></b>
Gain	$\uparrow$ 0.009	$\uparrow$ 0.008	$\downarrow$ 0.481

### C.2 Impact of Contrastive Loss at Different Feature Resolutions

We further investigate whether incorporating the contrastive loss  $\mathcal{L}_{con}$  at different feature resolutions can improve the model performance on the HMC-QU dataset. We gradually combine intermediate features from resolutions  $r \in \{4, 8, 16, 32\}$ . As shown in Table 11, the performance is promoted by gradually incorporating resolutions from  $r = 4$  to  $r = 16$ . Nevertheless, the performance decreases when

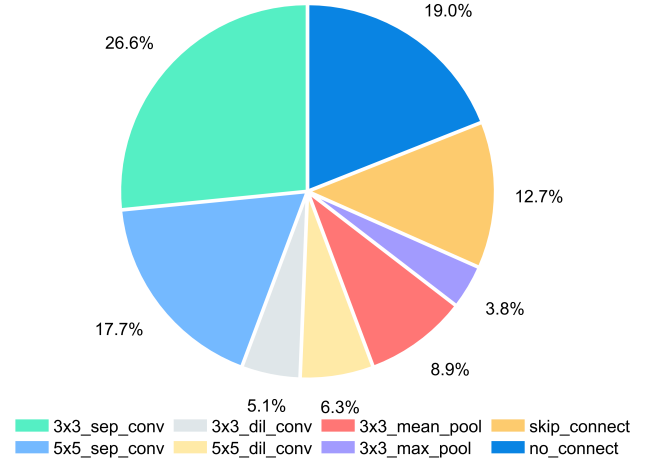


**Figure 12: The proportion of each candidate operation in the cells of the encoder NAS of the final searched network on the CETUS dataset.**

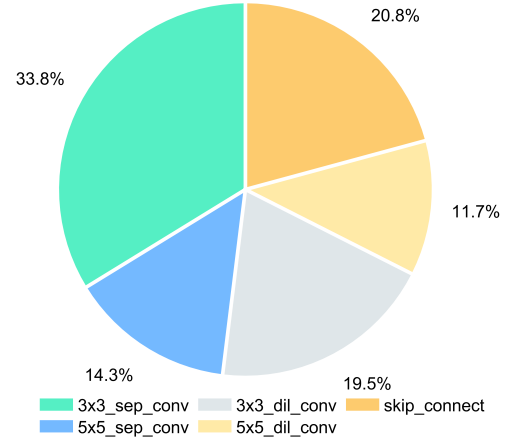


**Figure 13: The proportion of each candidate operation in the cells of the decoder NAS of the final searched network on the CETUS dataset.**

leveraging the  $r = 32$ . This is mainly because feature maps at  $r = 32$  contain high-level semantic information but lack detailed information necessary for contrastive analysis, and then the loss computed at this resolution does not contribute to the improvement.

## D MORE HYPER-PARAMETER STUDIES

To evaluate the effect of the number of network layers  $L$ , the network is initialized with 4, 6, and 8 layers, respectively, while maintaining the other parameters constant to facilitate a fair comparison. The quantitative results obtained across the HMC-QU, CETUS, and CAMUS datasets are presented in Table 12. It can be observed that

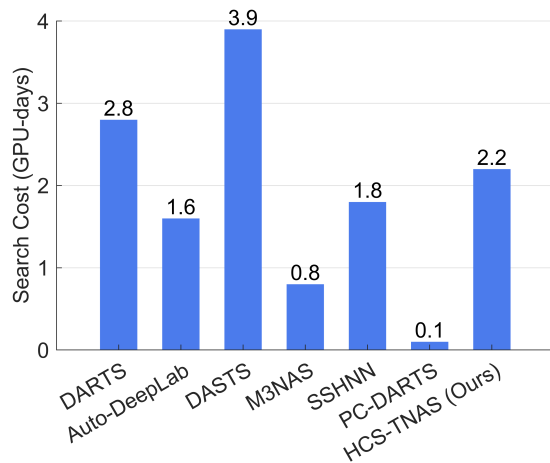


Figure 14: Comparison of search cost with the SOTA NAS frameworks on the HMC-QU dataset.

Table 11: Ablation Studies on different stages calculated in contrastive loss  $\mathcal{L}_{con}$  on the HMC-QU dataset.

Method	DSC $\uparrow$	IoU $\uparrow$	95HD $\downarrow$
None	0.924 <sub>(0.002)</sub>	0.922 <sub>(0.001)</sub>	2.852 <sub>(0.102)</sub>
$r \in \{4, 8\}$	0.929 <sub>(0.001)</sub>	0.928 <sub>(0.001)</sub>	2.603 <sub>(0.115)</sub>
<b><math>r \in \{4, 8, 16\}</math></b>	<b>0.933<sub>(0.002)</sub></b>	<b>0.931<sub>(0.002)</sub></b>	<b>2.480<sub>(0.161)</sub></b>
$r \in \{4, 8, 16, 32\}$	0.927 <sub>(0.002)</sub>	0.926 <sub>(0.001)</sub>	2.719 <sub>(0.148)</sub>

the proposed model employing 8 layers achieves superior performance in comparison to using 4 and 6 layers. Based on this finding,  $L$  in our model is initialized to 8.

Table 12: Hyper-parameter study on the impact of different numbers of network layers  $L$  on three datasets. The evaluation metric is IoU.

$L$	HMC-QU	CETUS	CAMUS
4	0.920 <sub>(0.002)</sub>	0.969 <sub>(0.002)</sub>	0.866 <sub>(0.002)</sub>
6	0.928 <sub>(0.001)</sub>	<b>0.978<sub>(0.002)</sub></b>	0.879 <sub>(0.003)</sub>
<b>8</b>	<b>0.931<sub>(0.002)</sub></b>	<b>0.978<sub>(0.001)</sub></b>	<b>0.884<sub>(0.003)</sub></b>

## E LIMITATIONS AND FUTURE WORK

We acknowledge certain limitations in our work. In Fig. 14, we compare the required architecture search time of HCS-TNAS with other SOTA NAS frameworks on the HMC-QU dataset, including DARTS [17], Auto-DeepLab [16], DASTS [32], M<sup>3</sup>NAS [18], SSHNN [7], and PC-DARTS [31]. We measure the execution time spent on the network search process, using a single Nvidia RTX 3090Ti GPU. Although we replaced the vanilla Transformer with EfficientViT as the NAS backbone to reduce GPU memory usage and training time, the search process is still time- and resource-intensive. In the present study, it takes approximately 2 GPU days to train the model. This is mainly attributed to the employed stage-wise optimization strategy, where additional time is required to update combination matrices for estimating network independence. While we plan to consider designing a more efficient optimization strategy in the future, we think that it also allows researchers to evaluate the computational requirements and potential trade-offs when selecting a suitable approach for a specific task or application.

Another direction for our future work is to enhance the generalization capabilities of our model. Specifically, while our current approach involves training on ultrasound image datasets, we aim to investigate the model’s transferability and robustness by evaluating its performance on other medical imaging modalities, such as magnetic resonance imaging (MRI) or computed tomography (CT) scans. This cross-modality research will provide insights into the model’s ability to generalize and adapt to diverse imaging data, which is crucial for practical clinical applications. By enhancing generalization across modalities, we strive to develop a more versatile and robust solution for medical image analysis workflows, ultimately contributing to improved patient care.